An electron spin-resonance study of Cr^{3+} in $LiSr_xCa_{1-x}AlF_6$ with x = 0, 0.5, 0.8, and 1

An electron spin-resonance study of Cr^{3+} in $LiSr_xCa_{1-x}AlF_6$ with $x = 0$, 0.5, 0.8, and 1

M Yamaga†, B Henderson‡, K Holliday§, T Yosida‖, M Fukui‖ and K Kindo¶

† Department of Electronics, Faculty of Engineering, Gifu University, Gifu 501-1193, Japan
‡ Department of Physics and Applied Physics, University of Strathclyde, Glasgow G1 1XN, UK
§ Department of Physics, University of San Francisco, 2130 Fulton Street, CA 94117-1080, USA
‖ Nakanihon Automotive College, Kamo 505-0077, Japan
¶ Research Centre for Materials Science at Extreme Conditions, Osaka University, Toyonaka 560-8531, Japan

Abstract. Electron spin-resonance (ESR) spectra of Cr^{3+} ions in $LiSr_xCa_{1-x}AlF_6$ crystals with $x = 0$, 0.5, 0.8, and 1 have been measured at X-band microwave frequencies in the temperature range 1.3–300 K. The intense ESR lines from Cr^{3+} ions in these crystals have been fitted to a trigonal spin Hamiltonian to determine values of the g-tensor ($g_\parallel$, $g_\perp$) and zero-field splitting, $2D$. The principal g-values ($g_\parallel \simeq g_\perp \simeq 1.974$) are almost the same in all cases whereas $2D$ increases sequentially for $x = 0$, 0.5, 0.8, and 1. The value of $|2D|$ for Cr^{3+}:$LiCaAlF_6$ decreases gradually as the temperature is increased from 1.3 K to 300 K. Over this same temperature range the value of $|2D|$ for Cr^{3+}:$LiSrAlF_6$ increases. The ESR spectra for Cr^{3+} in $LiSr_{0.5}Ca_{0.5}AlF_6$ and $LiSr_{0.8}Ca_{0.2}AlF_6$ are inhomogeneously broadened by discrete centres with pseudo-trigonal symmetry, different configurations of which correspond to the random occupation of the second-nearest-neighbour cation sites by Ca^{2+} and Sr^{2+} ions.

1. Introduction

There has been much recent interest in Cr^{3+}-doped colquiriite-type crystals as tunable gain media in the near infrared with potential for application in ultra-narrow-linewidth and femtosecond pulsed lasers [1]. The crystal growth, optical properties, and laser performance of Cr^{3+}-doped $LiCaAlF_6$ (LiCAF), $LiSrAlF_6$ (LiSAF), $LiSrGaF_6$ (LiSGaF), and $LiCaGaF_6$ (LiCGaF) have been reported in detail [1–9]. LiSAF host crystals provide larger absorption coefficients and a broader tuning range than LiCAF, determined by the strengths of static and dynamic distortions of the crystal field [5, 10, 11]. However, the thermal quenching of luminescence sets in at a lower temperature in LiSAF than LiCAF [12].

Assuming that their constituent atoms are perfect hard-sphere ions, the colquiriites can be treated as size-factor compounds, the structures of which are determined by the ratio r_-/r_+ of anion, r_-, and cation, r_+, radii [13]. Crystals that have r_-/r_+ in the range 1.37 to 2.41 have octahedral arrangements of anions around cations. In the colquiriites, the radius ratios are 1.80 (Li^+), 1.33 (Ca^{2+}) (1.15 (Sr^{2+})), and 2.51 (Al^{3+}), and all three cations are sixfold coordinated to nearest-neighbour F^- ions, even though the Ca^{2+} (and Sr^{2+}) ions lie outside the limiting radius ratios. The resulting distortions at the alkaline-earth sites vary from compound to compound and are accommodated elastically in (e.g.) LiCAF and LiSAF. In contrast, the distortion is so large in $LiBaAlF_6$ that the colquiriite structure is unstable.

As a consequence of their similar unit-cell sizes, LiCAF and LiSAF form a complete range of solid solutions, $LiSr_xCa_{1-x}AlF_6$ with $0 < x < 1$, in which the lattice constants c and a vary linearly with composition, x, in accord with Vegard's law [14]. The equilibrium diagram of LiCAF–LiSAF reveals a congruent melting composition $LiSr_{0.8}Ca_{0.2}AlF_6$ (LiSCAF-0.8), at which large single crystals were grown [15]. This compound was expected to combine in a single compound the apparent advantages of LiCAF and LiSAF, yielding larger absorption/emission cross sections and higher thermal quenching temperatures than for Cr^{3+}:LiSAF. Contrary to expectations, the luminescence quenching temperature for Cr^{3+}:LiSCAF-0.8 was almost equal to that of Cr^{3+}:LiSAF and its spontaneous decay rate was smaller than that of Cr^{3+}:LiSAF [12, 15]. Holliday *et al* [16] showed that substitutional Ca^{2+}/Sr^{2+} disorder in LiSCAF-0.8 had little effect on the optical spectra, concluding that the different lineshapes of Cr^{3+}-doped LiCAF and LiSAF are due to ionic relaxation in the excited electronic states being determined mainly by unit-cell sizes. The greater excited-state relaxation in LiSAF accords with the greater luminescence bandwidth and the large nonradiative decay rate induced by tunnelling between excited- and ground-state potential wells.

The ESR lines of the Cr^{3+} probe ions in $LiSr_xCa_{1-x}AlF_6$ crystals are expected to be inhomogeneously broadened by the disorder associated with the random distribution of Ca^{2+}/Sr^{2+} ions on dipositive cation sites. That the inhomogeneous broadenings of Cr^{3+} ESR lines in disordered $CaYAlO_4$ [17] and $Ca_3Ga_2Ge_4O_{14}$ [18] were attributed to discrete Cr^{3+} centres with different statistical configurations of randomly positioned cations in near-neighbour sites suggests that a similar analysis can be used to interpret the ESR spectroscopy of Cr^{3+}:$LiSr_xCa_{1-x}AlF_6$, even though randomly occupied sites in the latter compound are all occupied by ions of the same charge state unlike those in the former two. The disorder in $LiSr_xCa_{1-x}AlF_6$ occurs by Sr/Ca substitutions among the next-nearest cation neighbours of the $(AlF_6)^{3-}$ octahedron. The aims of the present study were to identify the ESR spectra of Cr^{3+} ions in the different octahedral configurations in these disordered crystals and measure their spin-Hamiltonian parameters in the $^4A_2$ ground state. The zero-field splittings, $2D$, of Cr^{3+} dopants in $LiSr_xCa_{1-x}AlF_6$ with $x = 0, 0.5, 0.8$, and 1 are reported and their consequences for the Cr^{3+} environment and optical properties of Cr^{3+}-doped colquiriite crystals are discussed.

2. Experimental details

The colquiriite crystal structure is trigonal, belonging to the space group D_{3d}^4. A schematic diagram of the unit cell is shown in figure 1. Cr^{3+} dopant ions substitute preferentially for Al^{3+} ions in trigonal sites with C_{3v} point group symmetry. Single crystals of Cr^{3+}:$LiSr_xCa_{1-x}AlF_6$ were grown from melts that contained 2 at.% of Cr^{3+} relative to Al^{3+} at compositions $x = 0, 0.5, 0.8$, and 1 by a modified Czochralski technique [19]. The mixed LiCAF–LiSAF crystals with $x = 0.5$ and 0.8 are labelled LiSCAF-0.5 and LiSCAF-0.8, respectively. The lattice parameters c and a listed in table 1 show that (LiCAF, LiSCAF-0.5, LiSCAF-0.8) and LiSAF, respectively, undergo compressive and extensive distortions along their trigonal axes [14, 19, 20].

Table 1. The lattice constants of LiCAF and LiSAF [14, 19, 20].

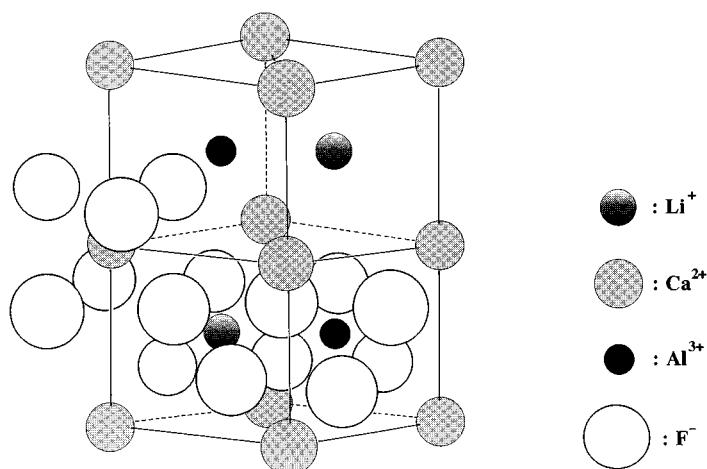| Crystals	LiCAF	LiSCAF-0.5	LiSCAF-0.8	LiSAF
Lattice constants (Å)				
a	4.996	5.05	5.07	5.084
c	9.636	9.85	10.1	10.21
$c/2a$	0.964	0.975	0.996	1.004

Figure 1. The crystal structure of LiCaAlF$_6$.

ESR spectra were recorded with a Varian X-band spectrometer using 270 Hz magnetic field modulation at temperatures in the range 1.3–300 K. The experimental samples were cut parallel to the $(10\bar{1}0)$, $(\bar{1}2\bar{1}0)$, and (0001) planes. The microwave frequency at and below 4.2 K was shifted to lower frequency than above 4.2 K because the cavity was immersed in liquid He. Temperatures above 4.2 K were achieved and controlled by a heater wound around the cavity, thereby evaporating liquid He from the ESR cavity but leaving liquid He at the bottom of the cryostat. The measurement temperature was monitored by a thermocouple set near the sample.

3. Experimental results

Figure 2 is a comparison of typical ESR spectra of Cr^{3+} ions in LiCAF, LiSCAF-0.5, LiSCAF-0.8, and LiSAF measured at a microwave frequency of $\sim$9.5 GHz with B parallel to the c-axis of the crystal and using $\sim$1 mW of power incident upon the cavity: the measurement temperature was 300 K. Since the ESR spectra of Cr^{3+} change substantially with composition it is appropriate to describe the spectra of pure compounds (LiCAF, LiSAF) and solid solutions (LiSCAF-0.5, LiSCAF-0.8) separately.

3.1. LiCAF and LiSAF

The ESR spectra of Cr^{3+}-doped LiCAF and LiSAF are typical of $S = 3/2$ ions in axial symmetry, consisting of lines due to the central $|\frac{1}{2}\rangle \leftrightarrow |-\frac{1}{2}\rangle$ transition and two fine-structure $|\pm\frac{1}{2}\rangle \leftrightarrow |\pm\frac{3}{2}\rangle$ transitions. Angular variations of the positions of these Cr^{3+} resonance lines in LiCAF and LiSAF crystals at 300 K are plotted in figure 3 for magnetic field rotations in the ac-plane: they are invariant under rotations in the (0001) plane (not shown). The orientation dependences of the resonance fields in figure 3 were analysed using an effective Hamiltonian appropriate to trigonal symmetry, i.e.

$$\mathcal{H} = \mu_B g_\parallel B_z S_z + \mu_B g_\perp (B_x S_x + B_y S_y) + D\left(S_z^2 - \frac{1}{3}S(S+1)\right) \tag{1}$$
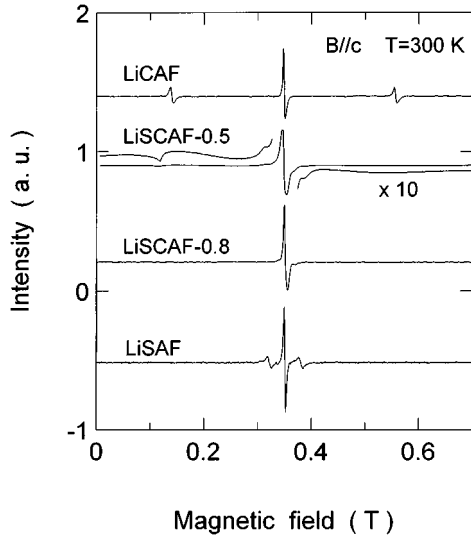
Figure 2. The ESR spectra of Cr^{3+} in LiCAF, LiSCAF-0.5, LiSCAF-0.8, and LiSAF measured with the magnetic field applied parallel to the c-axis at 300 K and at microwave frequencies of $\sim$9.50 GHz.
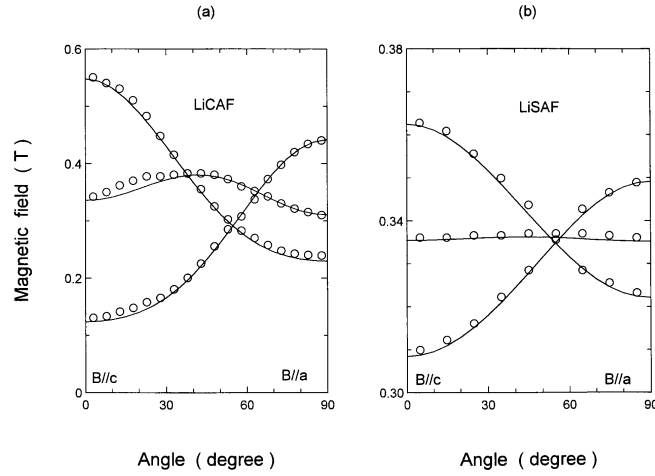

Figure 3. The angular dependence of the resonance lines of Cr^{3+} in (a) LiCAF with the microwave frequency of 9.276 GHz and (b) LiSAF with the microwave frequency of 9.273 GHz in the ac-plane at 300 K. Solid lines are calculated using equation (2).

where $S = \frac{3}{2}$ for a Cr^{3+} ion, $|2D|$ is the splitting between the $M_S = \pm\frac{1}{2}, \pm\frac{3}{2}$ levels in zero magnetic field, and μ_B is the Bohr magneton [21]. The principal z-, x-, and y-axes, respectively, of the spectra are the $\langle 0001 \rangle$, $\langle 10\bar{1}0 \rangle$, and $\langle \bar{1}2\bar{1}0 \rangle$ directions of the crystal. The resonance fields for the $|M_S - 1\rangle \rightarrow |M_S\rangle$ transitions in figure 3, calculated using equation (1) to second order in perturbation theory, are

$$B = B_0 - \frac{D}{2}(3\cos^2\theta - 1)(2M_S - 1) + \frac{D^2}{2B}\sin^2\theta\cos^2\theta[4S(S+1) - 24M_S(M_S - 1) - 9]$$

$$- \frac{D^2}{8B}\sin^4\theta[2S(S+1) - 6M_S(M_S - 1) - 3] \tag{2}$$

in which $B_0 = h\nu/g\mu_B$, $g \simeq g_\parallel \simeq g_\perp$, and θ is the angle between the principal z-axis of the spectrum and the magnetic field direction [21, 22]. The full curves in figure 3, calculated using equation (2) with the g- and $2D$-values given in table 2, are in good agreement with the experimental points.

Table 2. Spin-Hamiltonian parameters for Cr^{3+} measured for the colquiriite crystals at 300 K.

Crystals	LiCAF	LiSAF	LiSCAF-0.5	LiSCAF-0.8
$g_\parallel$	1.974(1)	1.974(1)	1.974(1)	1.974(1)
$g_\perp$	1.974(2)	1.974(2)	1.974(2)	1.974(2)
$2D$ (10^{-4} cm^{-1})	−2020(10)	270(10)	**a**: −1200*	
			b: −300*	
			c: −140*	**c**: −140*
				d: −40*

* The sign of $2D$ is assumed to be negative from the data in figure 8—see later—and its value is calculated assuming that the centre shows axial symmetry along the c-axis.

In figures 4(a) and 4(b), respectively, are shown the effects of temperature in the range 1.3 K to 300 K on the ESR spectra of Cr^{3+} ions in LiCAF and LiSAF. The widths and shapes of the ESR lines of Cr^{3+}:LiCAF do not change with temperature. There is, however, a small decrease in the fine-structure splitting of the $\Delta M_S = \pm\frac{1}{2} \leftrightarrow \pm\frac{3}{2}$ lines with increasing temperature from 4.2 to 300 K in LiCAF. As the temperature decreases from 4.2 K to 1.3 K the ratio of the intensities of the low-field line to high-field line increases from 1 to 1.2, showing that the $|\pm\frac{3}{2}\rangle$ spin sub-level is lowest in zero field and $2D$ is negative. In contrast, this intensity ratio for Cr^{3+}:LiSAF in figure 4(b) is less than unity at 1.3 K, confirming that in LiSAF $2D$ is positive. In contradistinction to the case of LiCAF, the Cr^{3+} fine-structure splitting in LiSAF increases with increasing temperature from 1.3 to 273 K. Between 1.3 and 4.2 K the ESR lines of Cr^{3+}:LiSAF shift to lower magnetic fields compared with those observed between 103 K
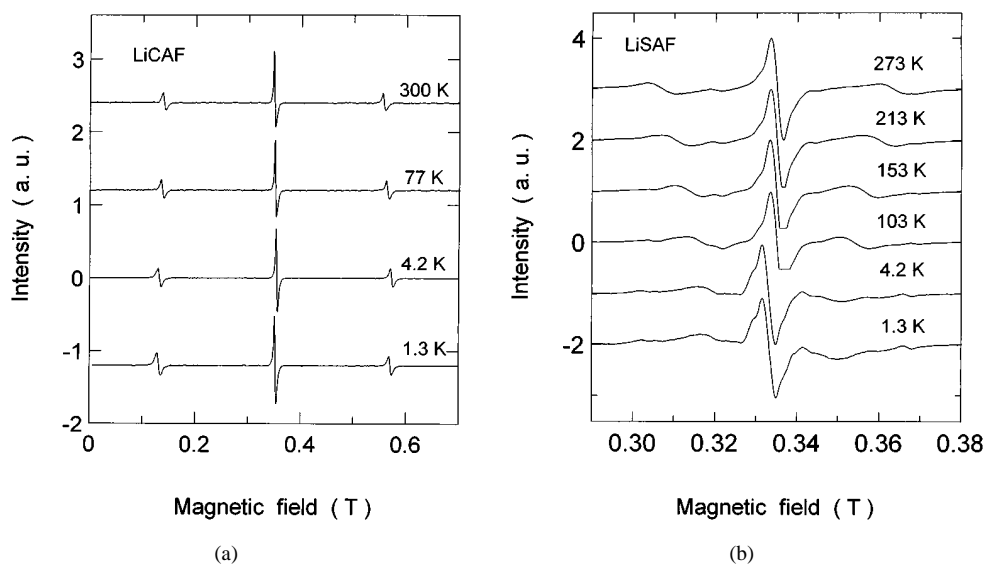

Figure 4. The temperature dependence of the ESR spectra of Cr^{3+} in (a) LiCAF and (b) LiSAF with $B \parallel c$.

and 273 K because the cavity is immersed in liquid He.

At higher gain than was used to record the spectra of LiCAF and LiSAF in figure 2, several weak lines are observed at magnetic fields around 0.305–0.376 T as shown in figure 4(b). These lines do not change positions in the temperature range 1.3–273 K. Although the angular variation in the *ac*-plane could not be observed completely, it shows that the spectra have no axial symmetry, but orthorhombic symmetry. The intensity is weaker than those of the dominant components. In consequence, the weaker lines are not related to the main Cr^{3+} resonances reported above. They are assigned to weakly coupled Cr^{3+} pairs or to Cr^{3+} ions perturbed by nearby defects or trace impurities, as identified first in high-resolution optical spectroscopy of Cr^{3+}:LiCAF [23].

3.2. LiSCAF-0.5 and LiSCAF-0.8

The ESR spectra of the substitutional solid-solution crystals Cr^{3+}: $LiSr_xCa_{1-x}AlF_6$ show the expected consequences of crystalline disorder familiar from earlier studies on Cr^{3+}-doped $CaYAlO_4$ [17] and $Ca_3Ga_2Ge_4O_{14}$ [18]. The disorder in $LiSr_xCa_{1-x}AlF_6$ occurs by Sr/Ca substitutions among the next-nearest cation neighbours of the $(AlF_6)^{3-}$ octahedron. There are seven (m, n) configurations of the second-nearest-neighbour cations in the colquiriite structure, figure 1, in which the total number of Sr^{2+} (m) and Ca^{2+} (n) ions at these sites is $m + n = 6$. The calculated probabilities of the seven discrete Sr^{2+}/Ca^{2+} configurations (m, n) in the $LiSr_{0.5}Ca_{0.5}AlF_6$ and $LiSr_{0.8}Ca_{0.2}AlF_6$ solid solutions are stated in table 3. The ordered arrangements $(0, 6)$ and $(6, 0)$ are the only incumbents of pure LiCAF and LiSAF, respectively. Configurations having large probabilities are $(2, 4)$, $(3, 3)$, and $(4, 2)$ in LiSCAF-0.5, and $(4, 2)$, $(5, 1)$, and $(6, 0)$ in LiSCAF-0.8. Although these configurations are expected to cause quite small changes to the ground-state energy levels, ESR spectroscopy can resolve the small energy differences that are manifest as the zero-field splittings (i.e. equations (1) and (2)). In consequence those configurations that have large probabilities are expected to have identifiable ESR spectra.

Table 3. The probabilities of the configurations with *m*th Sr^{2+} and *n*th Ca^{2+} ions ($m + n = 6$) in $LiSr_xCa_{1-x}AlF_6$ with $x = 0.5, 0.8$.

(m, n)	$x = 0.5$	$x = 0.8$
$(0, 6)$	0.016	0.0
$(1, 5)$	0.094	0.002
$(2, 4)$	0.234	0.015
$(3, 3)$	0.312	0.082
$(4, 2)$	0.234	0.246
$(5, 1)$	0.094	0.393
$(6, 0)$	0.016	0.262

The comparison of the ESR spectra of the four crystals in figure 2 shows the broadening of the central resonances for LiSCAF-0.5 and 0.8 with vestiges of additional structure on the shoulders of these lines. These features are clearer in the room temperature spectra of LiSCAF-0.5 and LiSCAF-0.8, figures 5(a) and 5(b), measured at several orientations in the *ac*-plane. The intense central line in the spectra of LiSCAF-0.5 and LiSCAF-0.8 measured along the *c*-axis is a composite from the $\Delta M_S = -\frac{1}{2} \rightarrow +\frac{1}{2}$ transitions of all configurations present in the samples. In this orientation the central line measures the value of $g_\parallel$, which will vary little between different configurations because it is determined by spin–orbit coupling for Cr^{3+} and by covalent spin transfer from neighbouring F^- ligand ions, identical features in all
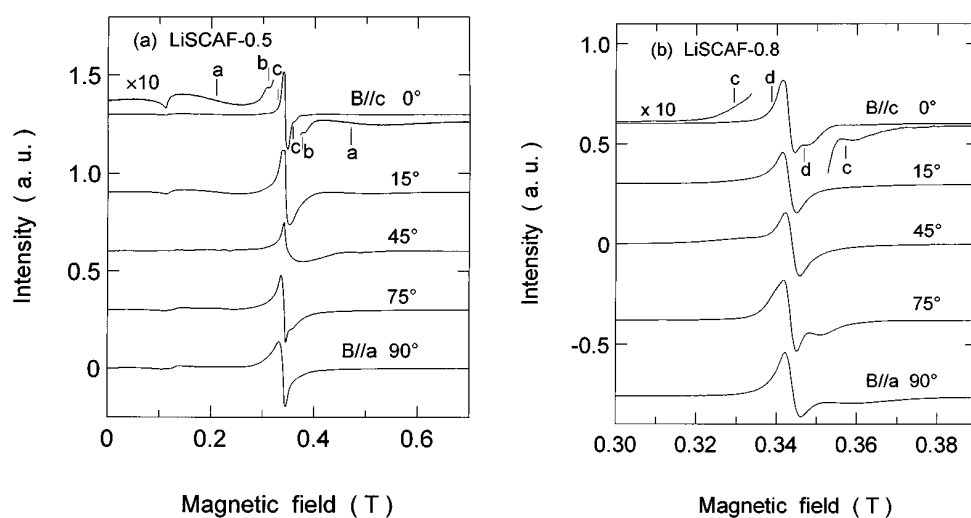
Figure 5. The angular variations of the ESR spectra of Cr^{3+} in (a) LiSCAF-0.5 and (b) LiSCAF-0.8, measured with the magnetic field applied in the ac-plane.

configurations.

On an expanded intensity scale, the ESR spectrum of LiSCAF-0.5 in figure 5(a) reveals much broader fine-structure lines **a** at lower and higher fields and additional structure (**b**, **c**) around the intense central line near 0.35 T. The widths $\sim$120 mT of the fine-structure **a** lines, being defined as the peak-to-peak separation, are much broader than those for LiCAF and LiSAF ($\sim$5 mT). Although their complete angular variations in the ac-plane of LiSCAF-0.5 crystals could not be determined because of this inhomogeneous broadening, each spectrum has characteristic behaviour. The **a** lines shift slightly toward the central line when the magnetic field is rotated through an angle $\theta = 15°$ from the c-axis. A single broad line extending to higher field is observed when the field is rotated with $\theta = 45°$ from the c-axis towards the a-axis. The spectrum when $\theta = 90°$ ($B \parallel a$) is asymmetric with a tail to lower field. This feature is expected to be similar to that in the case of LiCAF, figure 3(a), assuming that central and fine-structure lines are unresolved because of the large inhomogeneous broadening. Second-order splittings proportional to $3D^2/8B_0$, which vary as a function of the angle θ from the c-axis, equation (2), have the effect of distorting the lineshape in off-axis orientations (figure 5(a)). Hence the Cr^{3+} centre responsible for the **a** lines may be pseudo-trigonal symmetry. The principal z-axis, defined by the maximum measured separation of the fine-structure lines, is close to the c-axis of the crystal. The value of $|2D|$ for the **a** lines indicated in figure 5(a) is estimated to be $\sim$1200 $\times$ 10^{-4} cm^{-1}, in table 2, from the separation, $|4D|$, of the fine-structure lines observed with $B \parallel c$. The other fine-structure lines around $B \sim 0.33$ T (**b** and **c**) are observed only near $B \parallel c$, indicating that some geometrically inequivalent centres become magnetically equivalent in this orientation. However, the inhomogeneous widths of the ESR lines are much larger than the fine-structure separations, so the angular dependences of the fine-structure components could not be measured in the ac-plane and the (0001) plane. Such inhomogeneous broadening as there is may be caused by a distribution of fine-structure parameters and/or the tilting of the principal z-axis away from the c-axis of the crystal. The lower symmetry in these cases requires more general Zeeman ($g_{x,y,z}$) and fine-structure (D, E) terms in the spin Hamiltonian. However, since the g-tensor and fine-structure anisotropies are

small for **b** and **c**, their values of $|2D|$ for the Cr^{3+}:LiSCAF-0.5 can be estimated assuming axial symmetry about the c-axis with $g = g_\parallel = g_\perp$ and $E = 0$. The estimated values of g and $2D$ for the three distinguishable spectra **a**, **b**, and **c** of Cr^{3+}:LiSCAF-0.5 are summarized in table 2.

In the ESR spectrum of LiSCAF-0.8, figures 2 and 5(b), the fine-structure covers the field range 0.30–0.39 T and overlaps the intense central line. The Cr^{3+} fine-structure components **a** and **b** observed in LiSCAF-0.5 with $B \parallel c$ in figure 5(a) are not present in LiSCAF-0.8. However, an intense central line is observed in figure 5(b) attended by weak fine-structure lines **c** and **d**, as evidence that several distinct configurations also exist in these disordered LiSCAF-0.8 crystals. The spectra in figure 5(b), showing the clearly resolved central line with fine-structure components **c** and **d**, is almost isotropic against rotations in the ac-plane. In accord with equation (2), the isotropy implies that $|2D|$ is much smaller in configurations with large Sr^{2+} content. Within experimental error the resonance positions of the **c** lines in LiSCAF-0.8 and LiSCAF-0.5, table 2, are equal. Estimated values of g and $|2D|$ for the pseudo-trigonal centres appropriate to the **c** and **d** spectra in figure 5(b) were made in the same way as for the **b** and **c** spectra of LiSCAF-0.5 in figure 5(a) and are summarized in table 2.

Figure 6 shows the ESR spectra of LiSCAF-0.8 measured at 300, 77, and 4.2 K with microwave powers of 4, 4, and 1.5 mW and at microwave frequencies of 9.504, 9.520, and 9.305 GHz, etc. The fine-structure components **c** and **d** are evident in the spectrum at 4.2 K. The lineshapes of the observed spectra in the range 77–300 K do not change, but the width of the central line is smaller than at 4.2 K. In order to examine this effect, the microwave power dependence of the ESR spectrum was measured at 4.2 K between 0.1 and 10 mW (figure 7). The ESR spectrum measured at the lowest microwave power, 0.1 mW, is the same as it is at 300 K measured with 4 mW, confirming that in LiSCAF-0.8 the two Cr^{3+} centres related to fine-structure lines **c** and **d** have different spin–lattice relaxation rates.

To summarize, different fine-structure components in the ESR spectra of Cr^{3+}-doped LiSCAF-0.5 (labelled **a**, **b**, and **c** in figure 5(a)) and LiSCAF-0.8 (labelled **c** and **d** in figure 5(b))
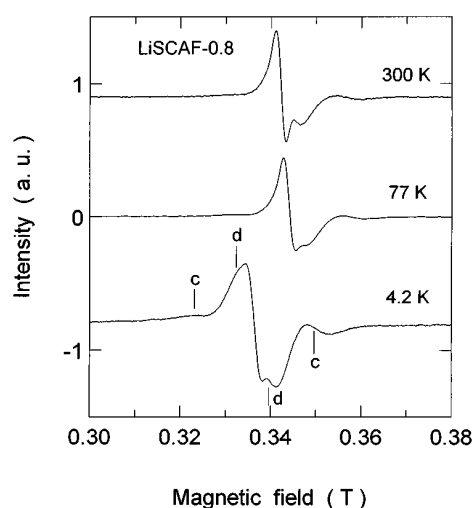

Figure 6. The temperature dependence of the ESR spectra of Cr^{3+} in LiSCAF-0.8 with $B \parallel c$.
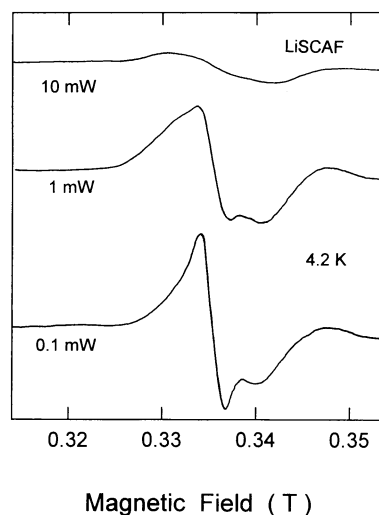
Figure 7. The microwave power dependence of the ESR spectra of Cr^{3+} in LiSCAF-0.8 measured with $B \parallel c$ at 4.2 K.

are evidence that several distinct statistical configurations of the neighbouring environment of the $(CrF_6)^{3-}$ octahedron exist in these disordered crystals.

4. Discussion

4.1. The spin-Hamiltonian parameters and lattice distortion

In mixed ionic crystals the unit-cell sizes change quasi-continuously with composition according to Vegard's law. The electronic ground state is expected to change in like fashion while reflecting also the local ionic structure. Increasing the values of x in the mixed crystals $LiSr_xCa_{1-x}AlF_6$ increases the lattice constant c more than the lattice constant a as shown in table 1 [4, 19, 20]. In consequence, the trigonally distorted $(CrF_6)^{3-}$ octahedra change from compressed to extended at some value of the composition parameter, x.

Wannemacher and Meltzer [23] determined that $g_\parallel = 1.98 \pm 0.02$ and $2D = -(6.10 \pm 0.1)$ GHz for Cr^{3+} ions in LiCAF using fluorescence line-narrowing (FLN) measurements of the zero-phonon line of the $^4T_2 \rightarrow {}^4A_2$ emission. The sign and magnitude of $2D$ measured by means of FLN are consistent with the spin-Hamiltonian parameters measured by means of ESR and listed in table 2. The negative sign of $2D$ for LiCAF implies that the $(CrF_6)^{3-}$ octahedron is compressed along the c-axis [24]. In contrast, the sign of $2D$ in LiSAF is positive at 1.3 K, corresponding to an intrinsic trigonal extension of the $(CrF_6)^{3-}$ octahedron [24].

The ESR spectra in figures 5, 6, and 7 identify several distinct Cr^{3+} centres in the mixed crystals. The plot of $2D$ versus x is shown in figure 8(a) assuming that $2D$ is negative for all discrete (m, n) configurations in LiSCAF-0.5 and LiSCAF-0.8 crystals. In order to confirm this assumption, $2D$ is replotted in figure 8(b) as a function of $m/(m+n)$ for the assumed (m, n) configuration with $m + n = 6$, whence the data fall on a straight line. The probability of the configuration (m, n) as a function of composition x is $_{m+n}C_m x^m (1-x)^n$, which has a peak in the distribution at the composition $x_p = m/(m+n)$. Hence, the value of $m/(m+n)$ for a particular configuration (m, n) corresponds to the composition, x_p, at which this configuration is most probable. In consequence, the linear variation of $2D$ with $m/(m+n)$ in figure 8(b) indicates that the zero-field splittings of the different configurations in the solid solution $LiSr_xCa_{1-x}Al_6$ obey a modified Vegard's law. As m increases, the value of $|2D|$ decreases; that is, the replacement

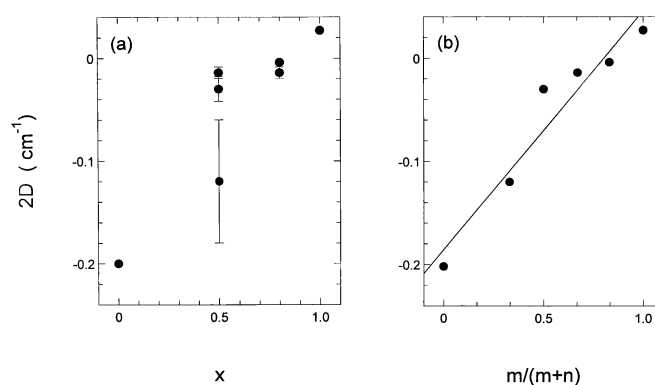**Figure 8.** (a) The relationship between the zero-field splitting $2D$ and x for $LiSr_xCa_{1-x}AlF_6$. The bars denote a distribution of $2D$ estimated from the inhomogeneous linewidths of the fine-structure lines. (b) $2D$ versus $m/(m + n)$ for the (m, n) configuration with $m + n = 6$. The straight line is calculated using the least-squares method.

of Ca^{2+} by the larger Sr^{2+} ion causes a gradual change in the distortion of the octahedron of F^- ions that surround the Cr^{3+} from compressed to stretched.

According to the temperature dependence of $|2D|$ for LiCAF, the intrinsic trigonal distortion of the octahedron decreases slightly with increasing temperature, remaining compressed along the c-axis up to 300 K, while the intrinsic trigonal distortion in LiSAF corresponds to a stretch along the c-axis which is enhanced at higher temperature. These results imply that $(AlF_6)^{3-}$ octahedra in LiCAF and LiSAF undergo a further stretching mode distortion in addition to the intrinsic distortion with increasing temperature.

4.2. Inhomogeneous broadening of ESR lines and substitutional disorder

The inhomogeneous broadening of the ESR lines of Cr^{3+}-doped LiCAF–LiSAF substitutional solid solutions is caused by the different statistical configurations of next nearest-neighbour ions of the $(CrF_6)^{3-}$ octahedra. The calculated probabilities of all (m, n) configurations in LiSCAF-0.5 and LiSCAF-0.8 crystals are summarized in table 3. Accordingly the most probable configurations are identified with the fine-structure lines **a**, **b**, and **c** in crystal LiSCAF-0.5 and with lines **c** and **d** in crystal LiSCAF-0.8. The large probabilities of the $(2, 4)$ and $(3, 3)$ configurations in LiSCAF-0.5 ($x = 0.5$), which are much reduced for LiSCAF-0.8 ($x = 0.8$), are assigned to the spectra **a** and **b**, respectively. Apart from the calculated probabilities (table 3), this assignment follows from table 2 and figure 8 in which the largest number of neighbouring Ca^{2+} in the configuration (i.e. $(2, 4)$), results in the largest zero-field splitting $2D \sim -1200 \times 10^{-4}$ cm^{-1}. The further assignment can then be made that the Cr^{3+} ions in configuration $(4, 2)$ give rise to lines **c** with $2D \sim -140 \times 10^{-4}$ cm^{-1}. There are three distinct arrangements of the Ca^{2+} and Sr^{2+} ions in configurations $(2, 4)$ and $(4, 2)$, which reduce the symmetry of the $(CrF_6)^{3-}$ octahedron to pseudo-trigonal. Since there is a common principal z-axis for the ESR spectra of these configurations, the c-axis of the crystal, these geometrical differences will contribute mainly to shifts and widths of the ESR lines in off-axis orientations. The three low-symmetry arrangements of the $(3, 3)$ configurations also contribute to spectra away from the c-axis orientation and for similar reasons.

The probabilities of ordered configuration $(0, 6)$ and $(6, 0)$, corresponding to the pure compounds LiCAF and LiSAF, respectively, are too small to be detected by means of ESR in LiSCAF-0.5, as are the configurations $(1, 5)$ and $(5, 1)$ (see table 3). However, the probability (0.26) of the $(6, 0)$ configuration in LiSCAF-0.8 is large enough that its ESR spectrum should have significant intensity. However, it is not apparent in figures 5(b), 6, and 7. The probability of the $(6, 0)$ configuration in the congruent melting composition may be reduced, perhaps due to local packing difficulties. The composition of this solid-solution crystal ($x = 0.8$) is close to that in figure 8(a) at which $2D = 0$ and the structure is almost octahedral. In that case the ESR spectrum will consist of lines from $|\frac{1}{2}\rangle \leftrightarrow |-\frac{1}{2}\rangle$ and $|\pm\frac{1}{2}\rangle \leftrightarrow |\pm\frac{3}{2}\rangle$ transitions overlapping the intense central line at $g = g_\parallel$ from other configurations, with very little orientation anisotropy. Fine-structure **c** lines in figures 5(b) and 6, identified for LiSCAF-0.5 with the $(4, 2)$ configuration, are similarly identified for LiSCAF-0.8. Since the lattice constants of the two compounds are different, it is anticipated that the value of $|2D|$ for the $(4, 2)$ configuration will be larger for LiSCAF-0.5 than for LiSCAF-0.8. Inaccuracies in determining $|2D|$, given the overlap and linewidths of the spectra, imply that the differences fall within the experimental error on $|2D|$, quoted in table 2 as $2D \sim -140 \times 10^{-4}$ cm^{-1}. The configuration with the largest probability (0.393) in LiSCAF-0.8 is $(5, 1)$, assigned to fine-structure lines **d** by virtue of their greater intensity than the **c** line and the smaller value of $2D \sim -40 \times 10^{-4}$ cm^{-1} which follow from the increased Sr^{2+} content in this configuration. Finally, disorder reduces the spin–lattice relaxation between the Cr^{3+} spin sub-levels. Saturation of the ESR spectrum

of Cr^{3+} in LiSCAF-0.8 shows that spin–lattice relaxation of the **c** levels is weaker than that of the **d** levels, giving rise to the greater linewidth of the fine-structure lines of the **c** spectrum.

4.3. Implications for optical spectra

The ground-state ESR spectra reveal crystal-field splittings of the ground state that result from an even-parity stretch or compression along the *c*-axis of the crystal. X-ray structure analysis shows that each of the MF_6 octahedra in figure 1 undergo even-parity (T_{2g}) and odd-parity (T_{1u}, and T_{2u}) distortions [20]. The T_{2g} distortion causes the splitting of the $^4A_2$ ground state measured by means of ESR. Since $2D < 0$ for LiCAF there is a compression along the trigonal axis, whereas $2D > 0$ for LiSAF, corresponding to an elongation of the trigonal axis [24]. This even-parity axial distortion also splits the excited $^4T_2$ and $^4T_1$ states, and by much more than the ground state; these splittings may be obscured by vibronic broadening and other effects [25]. Since there is a compressive distortion along the *c*-axis in LiCAF the $^4A_1(^4T_2)$ level is below $^4E(^4T_2)$ whereas in LiSAF $^4A_1(^4T_2)$ is above $^4E(^4T_2)$. The magnitude and sign of the $^4A_1(^4T_2)$–$^4E(^4T_2)$ splitting can be measured from the difference in the π- and σ-polarized first moments of the broad bands [25].

The optical band shapes are not much affected by disorder [16] mainly because the Ca–Sr substitution occurs in the next-nearest-neighbour shells of cations and their consequences cannot easily be resolved by such low-energy-resolution techniques as optical absorption and luminescence. Nevertheless, the odd-parity distortions will determine the intensities of the polarized absorption and emission spectra in both ordered and disordered materials. This is illustrated by applying a molecular orbital calculation of the polarized transition rates [26] to the published optical spectra of LiCAF and LiSAF [27]. According to Yamaga *et al*, the $^4A_2 \rightarrow ^4A_1(^4T_2)$ transition is π-polarized and induced by the *z*-component of the T_{2u} distortion (i.e. $T_{2u}(z)$) alone. In contrast, the $^4A_2 \rightarrow ^4E(^4T_2)$ transition is σ-polarized and induced by both $T_{2u}(z)$ and $T_{1u}(z)$ distortions. Theoretically the π/σ intensity ratio is $A_\pi/A_\sigma = 4/(1 + 3a)$, in which a is the relative σ-intensity induced by the $T_{1u}(z)$ mode. The experimental intensity ratios, 1.5 for LiCAF and 2 for LiSAF, correspond to $a = \frac{3}{9}$ and $\frac{5}{9}$, respectively, confirming that the difference between LiCAF and LiSAF is in the relative strengths of the $T_{2u}(z)$ distortions. In emission, where $I_\pi/I_\sigma = 1.5$ and 2.8 for LiCAF and LiSAF, respectively, it is the π-polarized transition that is dominant (i.e. from $^4A_1(^4T_2)$). Hence, in LiCAF $^4A_1(^4T_2)$ is lower than $^4E(^4T_2)$ both before and after vibronic relaxation, whereas in LiSAF $^4E(^4T_2)$ is lower than $^4A_1(^4T_2)$ in the unrelaxed excited state but above $^4E(^4T_2)$ in the relaxed excited state.

Similar considerations will apply to the polarized optical absorption spectra of the LiCAF–LiSAF solid solutions, even though the optical band shapes are little influenced by the inherent disorder [16]. The polarizations of the main absorption features in LiSCAF-0.8 are opposite to those in LiCAF and LiSAF [15]. The σ-component of the polarized $^4T_2$ band and the π-component of the $^4T_1$ band are dominant. These polarizations are induced by $T_{1u}(z)$, $T_{2u}(x)$, and $T_{2u}(y)$ distortions [26]. The $T_{2u}(x)$ and $T_{2u}(y)$ distortions are strongly related to lower symmetry of the $(CrF_6)^{3-}$ octahedron in the solid solutions.

5. Conclusions

ESR measurements of Cr^{3+}-doped colquiriite crystals LiCAF, LiSCAF-0.5, LiSCAF-0.8, and LiSAF reveal that a small number of discrete statistical configurations can be identified in the solid-solution crystals LiSCAF-0.5, LiSCAF-0.8. Measurements of the various ESR spectra

show that the zero-field splitting $|2D|$ decreases with increasing Sr^{2+} content of the crystals and that the $(CrF_6)^{3-}$ unit achieves almost perfect octahedral symmetry in LiSCAF-0.8. The distortions of the octahedron have important consequences for the optical properties of these laser-active materials, although the optical spectra are not very sensitive to the details of the disorder apparent in the substitutional solid-solution crystals.

Acknowledgments

References

[1] Payne S A and Pollock C R (ed) 1996 *OSA Trends in Optics and Photonics on Advanced Solid State Lasers* vol 1 (Washington, DC: Optical Society of America)
[2] DeYoreo J J, Atherton L J and Roberts D H 1991 *J. Cryst. Growth* **113** 691
[3] Payne S A, Chase L L, Atherton L J, Caird J A, Kway W L, Shinn M D, Hughes R S and Smith L K 1990 *Proc. SPIE* **1223** 84
[4] Payne S A, Chase L L, Newkirk H W, Smith L K and Krupke W F 1988 *IEEE J. Quantum Electron.* **24** 2243
[5] Smith L K, Payne S A, Kway W L, Chase L L and Chai B H T 1992 *IEEE J. Quantum Electron.* **28** 2612
[6] Beaud P, Chen Y E, Chai B H T and Richardson M C 1992 *Opt. Lett.* **17** 1064
[7] Smith L K, Payne S A, Krupke W F, DeLoach L D, Morris R, O'Dell E W and Nelson D J 1993 *Opt. Lett.* **18** 200
[8] Beaud P, Richardson M C, Chen Y F and Chai B H T 1994 *IEEE J. Quantum Electron.* **30** 1259
[9] Balembois F, Druon F, Falcoz F, Georges P and Brun A 1997 *Opt. Lett.* **22** 387
[10] Payne S A, Chase L L and Wilke G D 1989 *J. Lumin.* **44** 167
[11] Lee H W H, Payne S A and Chase L L 1989 *Phys. Rev.* **39** 8907
[12] Stalder M, Bass M and Chai B H T 1992 *J. Opt. Soc. Am.* B **9** 2271
[13] Bowen H J M 1967 *Properties of Solids and their Atomic Structures* (London: McGraw-Hill)
[14] Chai B H T 1998 private communication
[15] Chai B H T, Lefaucheur J, Stalder M and Bass M 1992 *Opt. Lett.* **17** 1584
[16] Holliday K, Russell D L, Nicholls J F H, Henderson B, Yamaga M and Yosida T 1998 *Appl. Phys. Lett.* **72** 2232
[17] Yamaga M, Yosida T, Fukui M, Takeuchi H, Kodama N, Inoue Y, Henderson B, Holliday K and Macfarlane P I 1996 *J. Phys.: Condens. Matter* **8** 10 633
[18] Yamaga M, Macfarlane P I, Henderson B, Holliday K, Takeuchi H, Yosida T and Fukui M 1997 *J. Phys.: Condens. Matter* **9** 569
[19] Pham A, Lefaucheur J, Nicholls J F H, Lutts G and Chai B H T 1994 *OSA Proc. on Advanced Solid State Lasers* vol 15 (Washington, DC: Optical Society of America) p 178
[20] Viebahn V W 1971 *Z. Anorg. Allg. Chem.* **386** 335
[21] Abragam A and Bleaney B 1970 *Electron Paramagnetic Resonance of Transition Ions* (Oxford: Clarendon) p 430
[22] McGarvey B R 1966 *Transition Metal Chemistry* vol 3, ed R L Carlin (New York: Dekker) p 129
[23] Wannemacher R and Meltzer R S 1989 *J. Lumin.* **43** 251
[24] McGarvey B R 1964 *J. Chem. Phys.* **40** 809
[25] Henderson B and Imbusch G F 1989 *Optical Spectroscopy of Inorganic Solids* (Oxford: Clarendon) pp 409–31
[26] Yamaga M, Henderson B and O'Donnell K P 1990 *J. Lumin.* **46** 397
[27] Chase L l, Payne S A, Smith L K, Kway W L, Newkirk H W, Chai B H T and Long M 1989 *OSA Proc. on Tunable Solid State Lasers* vol 5 (Washington, DC: Optical Society of America) p 71